# Energy Conversion Efficiency of Nanofluidic Batteries: Hydrodynamic Slip and Access Resistance

Yu Yan,[†] Qian Sheng,[‡] Ceming Wang,[‡] Jianming Xue,*,[‡] and Hsueh-Chia Chang*,[†]

[†]Department of Chemical and Biomolecular Engineering, University of Notre Dame, Notre Dame, Indiana 46556, United States
[‡]State Key Laboratory of Nuclear Physics and Technology, School of Physics and Center for Applied Physics and Technology, Peking University, Beijing 100871, PR China

ABSTRACT: With asymptotic and numerical analyses, we systematically study the influence of slip length and access Ohmic resistance (due to pore-end field focusing and concentration polarization) on the energy conversion efficiency of pressure-driven electrolyte flow through a charged nanopore. Hydrodynamic slip reduces the percent of energy dissipated by viscous dissipation but, through electro-osmotic convective current, can also reduce the electrical resistance of the nanopore. Since the nanopore resistance is in parallel to the load-access serial resistance, the latter effect can actually reduce useful current through the load. These two opposing effects of slip produce specific and finite optimum values of surface charge density and ionic strength. The optimization offers explicit analytical estimates for the realistic parameters and suggests an upper bound of 50% conversion efficiency at the slip length of 90 nm and 35% for measured electro-osmotic flow slip lengths of about 30 nm for charged channels.
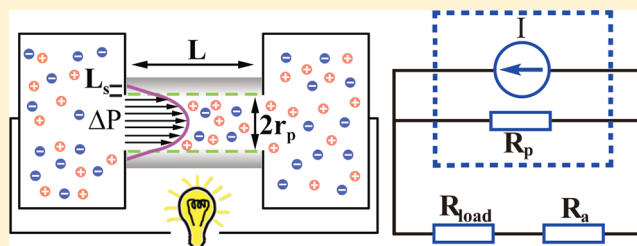
INTRODUCTION

Nanofluidic batteries are interesting energy generation systems for converting mechanical work into electrical power. Conversion of mechanical to electrical energy can be obtained by using acoustic phonons to drive condensed ions across a matrix to sustain a current. Ions can hop from site to site in a medium like Nafion[1,2] at a higher rate due to the phonon waves, or they can dissociate into the electrolyte in a nanopore due to the phonon waves and are then convected by the acoustically driven streaming flow.[3−7] However, phonon dissipation in a solid is very dissipative at a solid−liquid boundary, because of the high shear rate associated with IR frequencies of phonon vibration. Dissociation of condensed ions also requires significant energy. It is hence much more energy efficient if a DC or low-frequency pressure gradient is applied to drive electrolyte flow through a nanopore. If the nanopore radius is smaller than the Debye length, the charged double layers overlap, so there is a net charge within the electrolyte and a convective ion current, called the streaming current, that can be generated by steady pressure-driven flow. Depending on the load, the convected charge accumulates at the end of the pore to produce a streaming potential, which drives a field-driven current that opposes the streaming current. The streaming potential and its longitudinal field can also generate an electro-osmotic flow that opposes the driving pressure-driven flow. A transverse voltage drop also exists across the pore, but as long as the pore aspect ratio is large, coupling between the transverse field and longitudinal field can be neglected[8] such that the streaming potential is only responsible for the longitudinal field and the transverse field does not affect the streaming potential. Due to its simplicity,

harvesting electrical power with this nanofluidic battery system has gained considerable attention.

One of the challenges for the nanofluidic battery system is its low energy conversion efficiency. Up to now, the energy conversion efficiencies have been unacceptable: it is less than 1% for glass capillary systems,[9] 3.2% for the silicon nanochannel systems,[10] and around 5% for track-etched polyethylene terephthalate (PET) nanopores, which is the maximum value reported thus far.[11] Earlier theoretical studies that adjusted the surface charge density, geometric dimension, and salt concentration independently have reported a maximum efficiency of no more than 12%.[12−14] Such efficiencies are not high enough for practical applications, and it is of great interest to improve the energy conversion efficiency with systematic optimization that correctly accounts for the interplay among the parameters.

It has been suggested recently that a nanochannel with hydrodynamic slip, a nonzero relative motion between the fluid and the solid surface that has been shown to be true for some nanochannels with several layers of regimented water molecules at the surface and for hydrophobic surfaces with a separate air phase, nanobubbles, or a low-viscosity phase,[15−17] is the only means to improve the efficiency to over 20%. This is the result of a greatly reduced dissipative loss at the solid−liquid interface; hence, less mechanical work is needed to generate the same amount of streaming current. Slip lengths b from a few nanometers to micrometers have been measured for shear flow on hydrophobic surfaces,[16−20] but for electro-osmotic flow

(EOF) measurements, the maximum slip length is about 30 nm.[21] Nevertheless, Chang and Yang have theoretically demonstrated that when the slip ratio (b/a), of the slip length over the channel height, is greater than 0.7, the efficiency can be greatly improved to higher than 40%.[22] Pennathur et al. estimated, with a constant potential assumption, that the energy conversion efficiency could be as high as 35% when the slip length was 6.5 nm.[23] Davidson et al. predicted a value of about 30% with a slip length of 5 nm based on a thermo-electro-hydro-dynamic model.[24] Ren et al. found that the efficiency with a slip length of 6 nm was around 20%.[25]

Though large slip lengths of carbon nanotubes have been measured for some time (Majumder et al. reported a slip length of about 50 μm for a 7 nm diameter carbon nanotube,[26] and Whitby et al. measured a slip length of 35 ± 3 nm for a carbon nanotube with a diameter of 44 nm[27]), enhanced energy conversion with large-slip nanopores has yet to be reported. One possibility is that the large slip lengths have so far been measured mostly for uncharged hydrophobic carbon nanotubes and such surfaces might become hydrophilic, with much smaller slip lengths, when they are functionalized with surface charges,[28] a necessary condition for nanofluidic energy conversion. However, it has been shown with a surface force apparatus that charged mica surfaces can exhibit a slip length in excess of 20 nm if polymer molecules absorb onto the surface.[19] Recently, Bouzigues et al. report a slip length of 38 ± 6 nm for a 10 μm channel with a hydrophobic OTS-coated surface that sustains a strong EOF with its surface charge.[21] While such surface functionalizing means of endowing charged nanopores with large slip lengths have not been attempted for energy conversion, there is no reason why it cannot be done, in principle.

However, the earlier theories omit a key mechanism against high efficiency conversion that imposes a physical upper bound on the conversion efficiency for nanochannels with slip. The reservoir (access) resistance,[8,29−31] due to field focusing and concentration polarization[32−35] at the pore entrances, must be taken into account in determining the energy conversion efficiency at large slip lengths and load currents. Instead of viscous dissipation, which has been reduced for large slip lengths at the pore wall, limits on electric field flux and ion transport begin to bound the efficiency. Energy loss to thermal energy is no longer dominated by viscous dissipation but also to entropy generation during ion diffusion and Ohmic loss during ion electrophoretic motion. In fact, due to the parallel nature of the access Ohmic resistance and the nanopore electrical resistance, and the serial link between the access and load resistance, useful load current can be diverted toward the nanopore to reduce the efficiency with inefficient Ohmic loss there. This shorting of the load is quite possible, since reported measurements have shown that the access resistance can be comparable or larger than the nanopore resistance[14,31−35] and nanopore resistance has been shown to decrease rapidly with slip length.[25] This complex interplay will be shown to produce a specific optimum ion strength, for example, which is quite counterintuitive. Decreasing ion strength can reduce the percentage of co-ion within the nanopore and hence reduce the Ohmic loss to enhance efficiency in the high-concentration limit, but it can also increase the access resistance in the low-concentration limit to short the load current. It is important to note that this shorting occurs only if the nanopore electric resistance is much lower than the sum of the load and access resistance. Hence, the existence of the access resistance enhances this shorting mechanism and, in the absence of a load, becomes responsible for the short. With these two

opposite effects on the efficiency in two limits, the optimum ionic strength is hence a specific finite value with access resistance. With such complex interplay among a myriad of system parameters, optimization is best done systematically with the guidance of a theoretical model.

In the present work, we develop a theory and utilize a detailed numerical simulation to investigate the energy conversion mechanism in a cylindrical nanopore with slip. The nanopore is bounded by two larger reservoirs to mimic real experiments, allowing the existence of field focusing and access resistance. The optimized salt concentration, surface charge density, pore radius, and pore length, with proper account of the access resistance, suggest for properly functionalized charged nanopores a high conversion efficiency of 35% is possible with reported slip lengths.

MODEL SYSTEM AND EQUATIONS

The nanofluidic battery system we study is illustrated in Figure 1a. It contains two parts: a homogeneous charged cylindrical
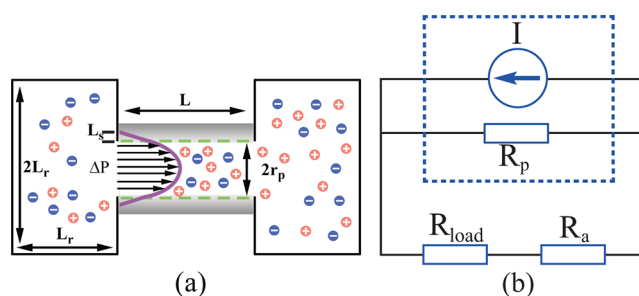

Figure 1. The system. (a) The model consists of a homogeneously charged nanopore and two reservoirs. r_p, L, and $L_s = b$ are the radius, length, and slip length of the charged nanopore, respectively. The two reservoirs have a cylindrical shape with equal length and radius L_r. (b) The equivalent circuit with R_p, R_{load}, and R_a being the nanopore, load, and access resistance, respectively.

nanopore and two reservoirs. Figure 1b displays the equivalent circuit of the nanofluidic battery, where R_p is the electrical resistance inside the nanopore, R_a is the access resistance of two reservoirs, which is due to field focusing of electrical field and concentration polarization at the pore entrances in the reservoirs[8,29−31] and external concentration polarization at high streaming current,[32−35] and R_{load} is the load resistance used to harvest the electrical power. The three parallel elements reflect the fact that the potential builds up at the downstream (relative to the pressure-driven flow) end of the nanopore due to the streaming current driven only by the pressure-driven flow, shown in the top element as a constant current source. This potential drives two opposite currents, one through the nanopore (middle element) against the streaming current and one through the pore entrance plus the load in series (bottom element). These two physically diverging currents form two parallel elements in the circuit model when the potential at the downstream pore entrance is used as one terminus. According to the classification in the circuit of Figure 1b, the nanopore current is due both to electrophoretic conduction and convection current due to EOF.

PNP (Poisson−Nernst−Planck) equations are used to describe the ion transport inside the nanopore. Here, we use C_i, z_i, and D_i to denote the concentration, the charge number, and the diffusion coefficient of species i (i = + for cation and i = − for anion), respectively. The PNP equations can be written as

$$\vec{J_i} = -D_i\left(\nabla C_i + \frac{F}{RT}z_i C_i \nabla\phi\right) \tag{1}$$

$$\nabla\cdot(\vec{J_i} + C_i\vec{u}) = 0 \tag{2}$$

$$\nabla^2\phi = -\frac{F}{\varepsilon}\sum_i z_i C_i \tag{3}$$

where $\vec{J_i}$ is the flux of species i due to the diffusion and electromigration and F, R, T, ε, and ϕ are the Faraday constant, the gas constant, the temperature, the dielectric constant of the medium, and the local potential, respectively. The flow velocity $\vec{u}$ is described with the incompressible Navier–Stokes (NS) equation as follows:

$$\nabla\cdot\vec{u} = 0 \tag{4}$$

$$\vec{u}\cdot\nabla\vec{u} = \frac{1}{\rho}[-\nabla P + \mu\nabla^2\vec{u} - (\sum_i Fz_i C_i)\nabla\phi] \tag{5}$$

where P, ρ, and μ are the pressure, the density, and the viscosity of the fluid, respectively.

In the model, the ion concentration at the two end reservoirs is set to the same bulk concentration C_0, the end of one reservoir is grounded at 0 V while the end of the other one is held at an external potential of ϕ_0. Details of the boundary conditions are given as follows:

At nanopore walls:

$$\nabla_\perp\phi = \frac{-\sigma}{\varepsilon}, \quad \vec{J_{i\perp}} = 0, \quad L_s = b, \quad i = +, - \tag{6}$$

At walls facing reservoirs:

$$\nabla_\perp\phi = 0, \quad \vec{J_{i\perp}} = 0, \quad \vec{u} = 0, \quad i = +, - \tag{7}$$

At left ends of reservoirs:

$$\phi = 0, \quad C = C_0, \quad P = p_0, \quad i = +, - \tag{8}$$

At right ends of reservoirs:

$$\phi = \phi_0, \quad C = C_0, \quad P = 0, \quad i = +, - \tag{9}$$

where p_0 is the applied pressure, b the slip length, and σ the amount of negative surface charge.

■ MATHEMATICAL ANALYSES

In our nanopore system, the flow rate Q and the current I have a linear Onsager dependence on the external pressure ΔP and voltage ΔV on the nanopore:[25,36−38]

$$I = S_{str}\Delta P + \frac{\Delta V}{R_p} \tag{10}$$

$$Q = \frac{\Delta P}{Z_p} + S_{str}\Delta V \tag{11}$$

where S_{str} is the streaming conductance and Z_p the hydrodynamic resistance. The Onsager reciprocity relationship $dQ/d\Delta V = dI/d\Delta P$ has been used in the above expression. The voltage and pressure drop are related through the simulation by $\Delta V = -((R_a + R_{load})/R_{load})\phi_0$ and $\Delta P = p_0$.

Poisson–Boltzmann equilibrium is used to resolve the concentration and potential profiles in the transverse direction of a nanopore with a radius of r_p. For a symmetric electrolyte with valency z, in cylindrical coordinate, the governing equation is

$$\frac{1}{r}\frac{d}{dr}\left(r\frac{d\varphi}{dr}\right) = \frac{\sinh(\varphi)}{\lambda_D{}^2} \tag{12}$$

where φ is the dimensionless potential normalized by the thermal potential (RT/Fz) and λ_D is the Debye length $\lambda_D = (\varepsilon RT/2z^2F^2C_0)^{1/2}$, with boundary condition $(d\varphi/dr)|_{r=0} = 0$ and $(d\varphi/dr)|_{r=r_p} = -(\sigma RT/\varepsilon Fz)$. For $\lambda_D \ll r_p$, the solution is the modified Bessel function of the first kind.[39] For $\lambda_D \sim r_p$, Petsev et al. were able to obtain an approximate analytical solution by matching the inner solution with the boundary layer.[40] For $\lambda_D \gg r_p$, an analytical expression can be obtained by assuming the counterion is the dominated ion.[22] Here we prefer to use a numerical solution, as our investigation includes all three regions.

The inertial term in the NS equation is negligible at low Reynolds number to yield the Stokes equation:

$$\mu\nabla^2 u(r) - \frac{\Delta V}{L}\frac{\varepsilon RT}{Fz}\nabla^2\varphi(r) + \frac{\Delta P}{L} = 0 \tag{13}$$

Hence, the velocity due to external pressure is

$$u_p(r) = \frac{\Delta P}{L}\frac{r_p{}^2}{4\mu}\left(1 - \frac{r^2}{r_p{}^2}\right) + \frac{\Delta P}{L}\frac{r_p b}{2\mu} \tag{14}$$

and the velocity due to electro-osmotic flow (EOF)

$$u_V(r) = \frac{\Delta V}{L}\frac{\varepsilon RT}{\mu Fz}(\varphi(r) - \varphi(r_p)) + \frac{\Delta V}{L}\frac{\sigma b}{\mu} \tag{15}$$

where the second term in both is due to hydrodynamic slip, with different scaling with respect to the pore radius. We note that the strongly nonlinear Poisson–Boltzmann equation in eq 12 preassumes the aspect ratio of the nanopore is large enough so that decoupling between the longitudinal and transverse field exists.[8] The transverse potential spans the entire volume of the nanopore that contains mobile ions, up to the Helmholtz–Stern plane with condensed ions. We hence neglect streaming current by condensed immobile ions in the above formulation and only consider the effective surface charge including the immobile ions. Electric field driven electron and ion currents by electron tunneling or ion hopping between sites in the Stern plane can also occur. However, since this current, represented by the pore resistance R_p in Figure 1b, drains useful current to the load, we shall minimize its effect by choosing materials with sufficiently low electron tunneling or ion hopping currents within the Helmholtz–Stern layer. Moreover, an interacting double layer in a nanopore can lead to counterion condensation and even charge inversion.[41] At low ionic strength, protonation and deprotonation at the surface become more prevalent.[10,42,43] The constant surface charge assumption may no longer be valid. However, we can also minimize this effect by a slight change in pH (carefully so that we do not change the ion strength significantly), as the surface charge is more sensitive to the pH than the bulk concentration.

The streaming conductance, pore resistance, and hydrodynamics resistance of the model in Figure 1 can now be formally expressed as follows:

$$S_{str} = \frac{\int_0^{r_p} 2\pi r\rho(r)u_P(r)\,dr}{\Delta P} \tag{16}$$

$$\frac{1}{R_p} = \frac{\int_0^{r_p} 2\pi r \left[\frac{\Delta V}{L} \sum_i C_i(r) \frac{z^2 F^2 D}{RT} + \rho(r) u_V(r) \right] dr}{\Delta V} \qquad (17)$$

$$\frac{1}{Z_p} = \frac{\int_0^{r_p} 2\pi r u_p(r) \, dr}{\Delta P} = \frac{\pi r_p^3 (r_p + 4b)}{8\mu L} \qquad (18)$$

where the ion concentration obeys Boltzmann equilibrium $C_{\pm} = C_0 \exp(\mp \varphi)$ and the space charge is $\rho(r) = Fz(C_+ - C_-)$. Here, convective current due to electro-osmotic flow (EOF), which is counter to the pressure-driven flow, is included in the second term of the expression for R_p.

From the equivalent circuit in Figure 1b, the potential across the nanopore is $\Delta V = -S_{str} \Delta P \{ [R_p(R_a + R_{load})]/(R_a + R_{load} + R_p) \}$. Hence, the efficiency of the energy conversion in this system is

$$\eta = \frac{\frac{\Delta V^2 R_{load}}{R_a + R_{load}}}{Q \Delta P} = \frac{\alpha(\chi - \beta)}{(1 + \chi)(1 + \chi - \alpha\chi)} \qquad (19)$$

where the dimensionless quantity $\alpha = S_{str}^2 Z_p R_p$ is called the figure of merit that measures the relative strength of electro-osmotic flow and pressure-driven flow,[36–38] $\chi = (R_a + R_{load})/R_p$ is the dimensionless total resistance excluding pore resistance, and $\beta = R_a/R_p$ is the dimensionless access resistance relative to the pore resistance. The efficiency is hence a function of three convenient dimensionless parameters with the equivalent circuit of Figure 1b. A contour of the efficiency as a function of dimensionless load resistance and access resistance for fixed $\alpha = 0.5$ is given in Figure 2a. The efficiency monotonically decreases with access
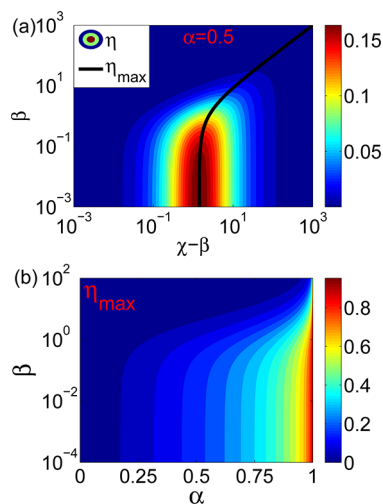

Figure 2. (a) Contour of efficiency as a function of normalized access resistance β and load resistance $\chi - \beta$ at $\alpha = 0.5$. The black line corresponds to the condition when maximum efficiency is achieved for each access resistance. (b) Contour of maximum efficiency as a function of figure of merit α and the dimensionless access resistance β. The maximum efficiency increases monotonically with α and decreases with β.

resistance, and there is an optimal load resistance. The maximum efficiency is achieved at $(d\eta/d\chi) = 0$ (line in Figure 2a) or

$$\chi - \beta = \frac{\sqrt{\beta^2(1 - \alpha)^2 + (1 - \alpha)(\beta(2 - \alpha) + 1)}}{1 - \alpha} \qquad \alpha \neq 1 \qquad (20)$$

The optimum load resistance increases with the access resistance. The figure of merit α must be less than unity due to energy conservation:[10] the total energy harvested on the load and access resistance cannot be more than mechanical energy.

Figure 2b shows the contour map of the maximum efficiency as a function of the figure of merit α and dimensionless access resistance β. It shows that the maximum efficiency monotonically increases with α and decreases with β. In fact, from eq 17, if the access resistance β is the same, at the same total load χ, the efficiency always increases with α, as the numerator increases while the denominator decreases, so the maximum efficiency must also increase with α. If the figure of merit α is fixed, with the same total load χ, the numerator decreases with increasing β and the access resistance always has a negative impact on the maximum efficiency. Hence, efficiency optimization corresponds to enhancing α and diminishing β. That slip enhances both, in the presence of access resistance, is a curious phenomenon for nanofluidic batteries that is responsible for finite optimum parameter values.

A few analytical limits are instructive. First, when the access resistance is much smaller than the pore resistance $\beta \ll 1$, eqs 19 and 20 become the same as those reported in earlier reports without access resistance.[10,25,36] For the opposite (but rather uninteresting) limits of $\beta \gg 1$ and $\beta \gg 1/(1 - \alpha)$, eq 19 becomes $\chi - \beta = \beta$. The maximum efficiency hence occurs when the load resistance is equal to the access resistance when the latter is large. In fact, when access resistance is much larger than pore resistance $\beta \gg 1$, the voltage across the nanopore $\Delta V \sim -S_{str} \Delta P R_p$ and the flow rate Q approach constant asymptotes at the limit of large access resistance, except at the singular limit of $\alpha \sim 1$ when Q approaches zero. The total input energy is hence constant, in the limit of large access resistance. The maximum efficiency and maximum power will be achieved under the same condition. This limit is similar to a constant voltage battery ΔV with a resistance R_a: the maximum power on the load can be attained when the load is the same as the access resistance. The corresponding energy efficiency is

$$\eta = \frac{\alpha\beta}{(1 + 2\beta)(1 + 2\beta - \alpha 2\beta)} \ll 1 \qquad (21)$$

which means the access resistance is responsible for such low-efficiency systems.

However, an interesting limit exists when $1/(1 - \alpha) \gg \beta \gg 1$ in Figure 2, when the figure of merit can be closer to unity. The maximum efficiency is then achieved at $\chi - \beta = (\beta/(1 - \alpha))^{1/2}$

$$\eta = \frac{\sqrt{\beta/(1 - \alpha)}}{(1 + \sqrt{\beta/(1 - \alpha)})} \sim 100\% \qquad (22)$$

In the case of extreme large slip length, the velocity profile driven by both pressure gradient and electro-osmosis is flat within the nanopore, as the slip velocity takes over in eqs 14 and 15. This mathematical limit simplifies the integration in eqs 16–18 to offer an analytical estimate of the figure of merit

$$\alpha \sim \frac{\left[\frac{u_p(r)}{\Delta P} \int_0^{r_p} 2\pi r \rho(r) \, dr \right]^2}{\left[\frac{u_V(r)}{\Delta V} \int_0^{r_p} 2\pi r \rho(r) \, dr \right] \left[\frac{u_p(r)}{\Delta P} \int_0^{r_p} 2\pi r \, dr \right]} = \frac{\frac{r_p b}{2\mu L} 2\pi r_p \sigma}{\frac{\sigma b}{\mu L} \pi r_p^2} = 1 \qquad (23)$$

in which the local electroneutral condition including surface charge has been used[8]

$$\int_0^{r_p} 2\pi r \rho(r)\, dr = 2\pi r \sigma \tag{24}$$

On the other hand, higher hydrodynamic slip increases the osmotic flow from eq 17 to reduce the pore resistance. As a result, the contribution of access resistance relative to pore resistance, as measured by β, increases and will eventually limit the favorable influence of the slip length on the efficiency.

■ OPTIMIZATION

We carry out a systematic numerical and theoretical optimization here, guided by the above analyses with respect to figure of merit α and dimensionless access resistance β. Other than the slip length, reservoir size, electrolyte concentration, surface charge density, pore radius, and pore length will all be scrutinized to optimize the conversion efficiency. A symmetric aqueous solution (KCl) is used, and the external pressure is fixed at 80 kPa unless otherwise specified. The diffusion coefficients of K^+ and Cl^- are assumed to be equal to 2×10^{-9} m^2/s.

We first investigate the role of reservoir size on the access resistance and total hydrodynamic pressure drop at the entrance and exit, separately. To simplify the problem, only the PNP equations are used to calculate the total resistance of the system: a 4 μm long cylindrical nanopore with a radius of 30 nm, surface charge density 10 mC/m^2, and a reservoir with the same length and radius are used. The result is evaluated at small voltage 0.01 V so that external polarization will not be important.

Without EOF, the pore resistance can be estimated by Donnan theory[8] $R_p = RTL/(z^2F^2D\pi r_p^2C_0(4 + X^2)^{1/2})$, where $X = 2\sigma/zFC_0r_p$. Figure 3a shows the ratio between total resistance and
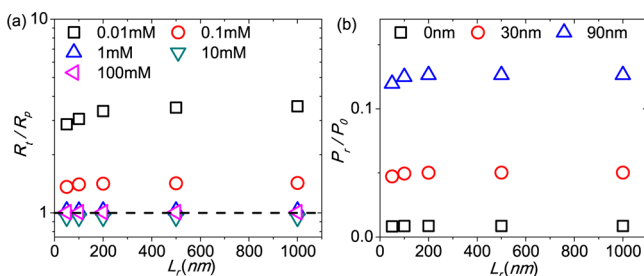

Figure 3. The influence of reservoir size on the access resistance and pressure drop within the reservoir, for a nanopore with a length of 4 μm, a radius of 30 nm, and a surface charge density of 0.01 mC/m^2. The reservoir has a length and radius of the same size L_r. (a) Five different concentrations are used; the total resistance approaches constant as the reservoir size increases. (b) The pressure drop for different slip lengths.

pore resistance; with the increase of the reservoir size, the total resistance increases monotonically but approaches a constant when the reservoir is much larger than the pore size. The access resistance for a cylindrical nanopore with uniform conductivity can be expressed as twice the Hall resistance:[8,29,30]

$$R_a = \frac{RT}{4z^2F^2Dr_pC_0} \tag{25}$$

where both the inlet and the outlet have been included. At high concentrations, the total resistance is close to the pore resistance. However, for small concentrations, the access resistance becomes important: at 0.01 (0.1) mM, the access resistance is 4.1 (0.41) times the pore resistance from eq 25, compared to 2.5 (0.42) from simulation. The overestimation at 0.01 mM is due to the fact that the high conductivity within the nanopore might

increase the conductivity near the access. However, it will be shown that eq 25 actually underestimates the access resistance due to external concentration polarization,[32−35] whose effect is not considered in eq 25 but will be scrutinized later.

Figure 3b shows the ratio of pressure drop due to the two reservoirs to the total applied pressure. The pressure drop is similar to that of flow through a circular aperture, which was first given by Sampson[44] $P_a = 3\mu Q/r_p^3$, where Q is the flow rate. Hence, its ratio to total pressure is

$$\gamma = \frac{3\mu/r_p^3}{3\mu/r_p^3 + Z_p} = \frac{3\pi(r_p + 4b)}{3\pi(r_p + 4b) + 8L} \tag{26}$$

The pressure drop due to the reservoirs hence increases with the slip length b, reaches about 12.6% of the total pressure drop (10.3% from eq 26) at a slip length of 90 nm, and approaches a constant when $L_r \gg r_p$. Also from eq 26, the reservoir pressure drop is insensitive to the pore radius when $b \gg r_p$ but is sensitive to the length and can be very high for short pores with large slip lengths.

However, if EOF is present to counter the pressure-driven flow, a higher pressure is necessary to drive the same flow rate and the reservoir contribution to the total pressure drop reduces to 4.1% for a 90 nm slip length without any load resistance. Since the highest reservoir contribution to pressure drop is only about 14.3% (for a 0.5 μm long nanopore) in our windows of interest, the contribution of the reservoir to the efficiency can be safely neglected in a first-order estimate of the optimal condition.

We next analyze the effect of the slip length b on the energy conversion efficiency η by varying the slip length from 0 to 90 nm, with the KCl concentration held constant at 1 mM, the surface charge density at 10 mC/m^2, the pore at a radius of 30 nm and the length at 4 μm, and the reservoir size 1 μm by 1 μm. In Figure 4 and all subsequent plots, the symbols are from numerical simulations, dashes from model without access resistance, and solid lines from model with access resistance. While the efficiency obviously increases with slip length, the increase saturates beyond a critical slip length due to access resistance. At low slip lengths b, the pore resistance R_p is not significantly reduced by EOF and slip definitely reduces the percent of energy loss due to viscous dissipation and increases the efficiency correspondingly. When the slip length is sufficiently large, however, $R_p \sim 1/b$, energy input (ΔPQ) and harvested energy ($\sim I^2R_p$) all scale as $1/b$ and the efficiency approaches 100% without access resistance. With access resistance, a different asymptote is approached, as the reduced R_p diverts current from the load-access element to the nanopore element. This saturation of efficiency due to access resistance will be an important factor when we optimize over the critical parameters of ionic strength and surface charge. We first calculate the dependence of the current I and the flow rate Q on the load resistance (by varying ϕ_0). Parts a and b of Figure 4 show that both I and Q decrease with the increase of load resistance and increase with the increase of slip length. According to the equivalent circuit of the nanofluidic battery system in Figure 1b, a larger load resistance means more current can pass through the pore itself; thus, the current on the load decreases (Figure 4a). Besides, a larger load resistance also causes a higher potential across the nanopore; thus, EOF becomes stronger. Since EOF counters pressure-driven flow, the total flow rate decreases (Figure 4b). The $\eta-R_{load}$ curves at different slip lengths are hence calculated by $\eta = I^2 * R_{load}/\Delta PQ$, as shown in Figure 4c, from which we get the maximum conversion efficiency.
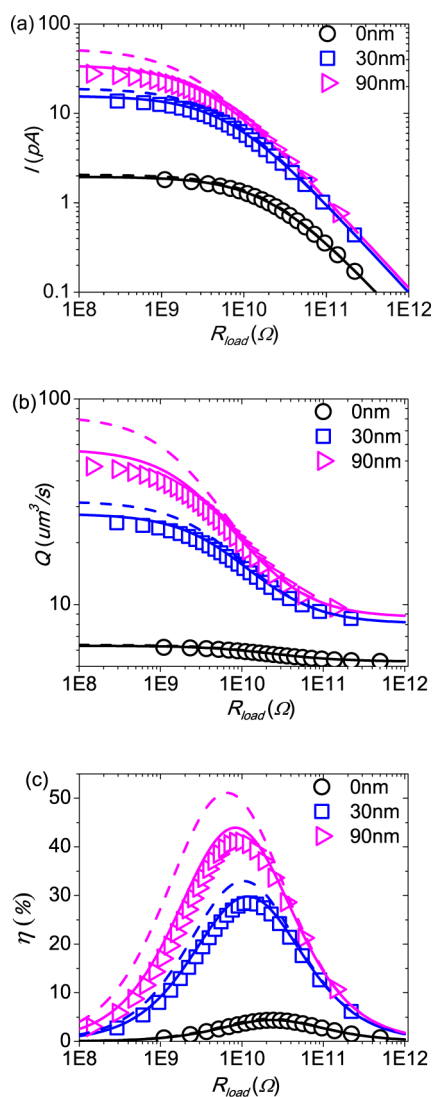
Figure 4. The dependence of the current I, flow rate Q, and energy conversion efficiency η on the load resistance: the symbols are from numerical simulations, dashes from the model without access resistance, and solid lines from the model with access resistance. Three different slip lengths are used: 0 nm (open black circles), 30 nm (open blue squares), and 90 nm (open magenta triangles).

Figure 4 also shows that, with the no-slip condition, the simulation and the two theoretical models with and without access resistance are very close to each other. In contrast, for nanopores with slip, the access resistance model is much closer to the simulation. The deviation of two theoretical models diminishes as R_{load} increases, as the influence of access resistance decreases at large R_{load}.

Figure 5 shows how the "measured" streaming current, pore resistance, access resistance, figure of merit, and maximum efficiency change for various slip lengths. As shown in Figure 5d, η_{max} increases rapidly when slip length is small but begins to saturate at larger slip lengths. The maximum efficiency in no-slip nanopores is only about 4.3%, compared to 41% when the slip length reaches 90 nm, which is about 9 times higher. The model without access resistance overestimates the maximum efficiency especially for large slip length. In fact, from our theory, the efficiency will reach 63 (94)% for 10 μm slip length with (without) access resistance. However, as shown earlier, the access pressure drop will be the dominant one at large slip

lengths and the actual efficiency will be very low as most of the pressure drop is wasted. Hence, there should be an upper bound for the efficiency at large slip lengths.

To delineate this mechanism in more detail, the access resistance is estimated by simulations at $\phi_0 = 0$ ($R_{load} = 0$): $R_a = U/I$, where U is the potential drop across the reservoirs. The nanopore resistance is then estimated by $R_p = -d\phi_0/dI - R_a$, where $d\phi_0/dI$ is the slope of the $\phi_0 \sim I$ curve. The values of R_a and R_p at different slip lengths are shown in Figure 5b. From simulations, R_a is only about 7% of R_p without slip and can hence be neglected. When the slip length increases, R_p decreases quickly due to EOF, but R_a remains roughly constant. When the slip length is 90 nm, R_p is only 2.22×10^9 Ohm while R_a is 1.62×10^9 Ohm, and they become comparable. Here, the pore resistance is very close to our prediction, but the access resistance is about 1.5 times the predicted value from eq 25. This is due to the external concentration polarization at high currents.[32−35] If we replace the analytical access resistance in our model with the value from simulation, a closer agreement with the simulation result can be achieved. However, the convenient closed-form analytical expression (eq 25) is sufficiently accurate and we shall continue to use it.

Figure 5a shows the "measured" streaming current as a function of slip length. Here, the "measured" streaming current is defined as the current when there is no load resistance but the access resistance remains, since, in reality, when the streaming current is measured, the access resistance is always present. Hence, the "measured" streaming current is defined as $I_{str} = S_{str}\Delta P/(1 + \beta)$, Without the access resistance, the "measured" streaming current becomes $I_{str} = S_{str}\Delta P$, which restores to the usual streaming current and increases linearly with slip length, since the extra velocity term in eq 14 is linear. Figure 5c shows β also increases linearly with slip length. This is because of the extra linear term in the osmotic flow expression of eq 15, such that $1/R_p$ and β both increase linearly with slip length. (As shown in Figure 5b, the access resistance is not a function of the slip length, as we have assumed in the theoretical estimate.)

The above results indicate that slip can greatly improve the energy conversion efficiency in a nanofluidic battery system, and larger slip length means higher energy conversion efficiency. However, when the slip length increases, the EOF effect will decrease the electrical resistance of the nanopore. Consequently, useful current will be diverted away from the load toward the nanopore when access to the pore resistance ratio is significant and the increase in η_{max} becomes less pronounced. Neglecting the access resistance will significantly overestimate the energy conversion efficiency.

This curious phenomenon of EOF reducing the useful load current by shorting the nanopore in the parallel circuit model of Figure 1b produces a profound effect of the salt concentration C_s on the energy conversion efficiency. In the next set of calculations, the salt concentration is varied from 0.01 to 100 mM, the pore radius is fixed at 30 nm, and the surface charge density is 10 mC/m². To study the influence of slip length on the salt concentration, three $\eta_{max} \sim C_s$ curves are calculated at slip lengths of 0, 30, and 90 nm. We note that a constant surface charge assumption is no longer valid at low concentrations.[10,42,43] However, the optimum concentration here is around 1 mM, so we can adjust the pH between 4 and 10 without introducing too many ions into the pore, to maintain the surface charge. Hence, we use the constant surface charge condition to optimize the concentration. Figure 6 shows that, at low concentrations, the nanopore resistance and the figure of
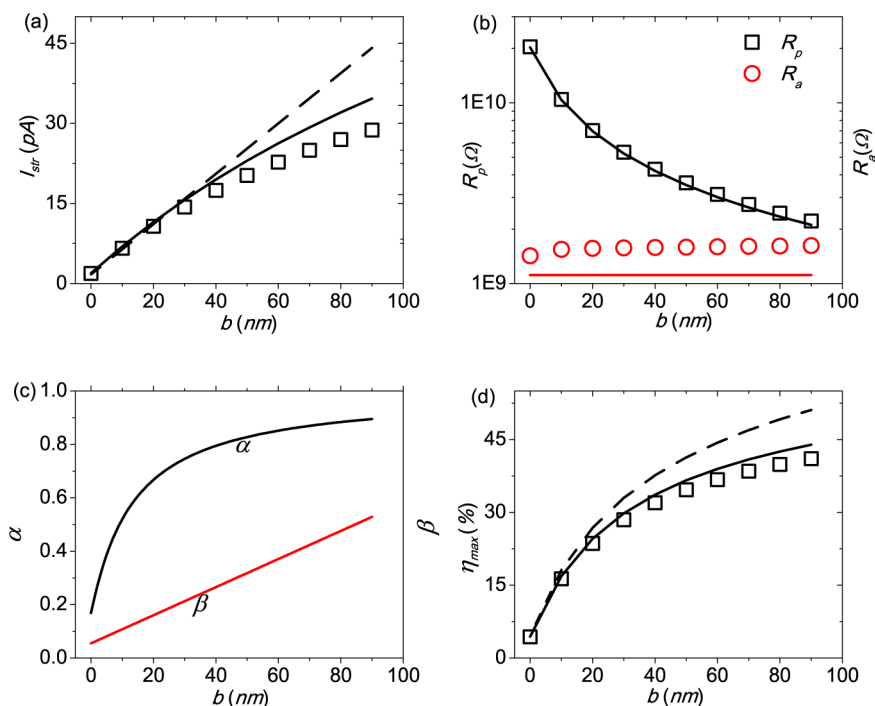
Figure 5. The dependence of the "measured" streaming current I_{str}, pore resistance R_p, access resistance R_a, figure of merit α, access resistance to pore resistance ratio β, and maximum efficiency η_{max} on the slip length b: the symbols are from numerical simulations, the dashes from the model without access resistance, and the solid lines from the model with access resistance.
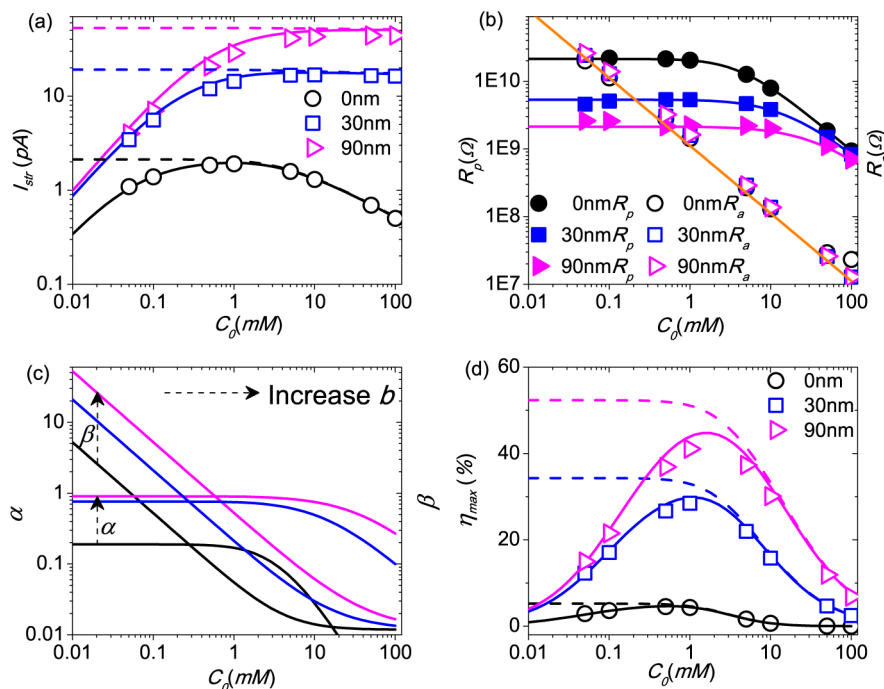

Figure 6. The dependence of the "measured" streaming current I_{str}, pore resistance R_p (closed symbols, lines), access resistance R_a (open symbols, orange line), figure of merit α, access resistance to pore resistance ratio β, and maximum efficiency η_{max} on the concentration C_0: the symbols are from numerical simulations, the dashes from the model without access resistance, and the solid lines from the model with access resistance. Three different slip lengths are used: 0 nm (black circles), 30 nm (blue squares), and 90 nm (magenta triangles). A finite optimum ionic strength occurs with the introduction of access resistance.

merit approach constant asymptotes, while the access resistance increases with decreasing concentration, as it is inversely proportional to the concentration. Hence, the ratio of access resistance to nanopore resistance β increases, which from our contour map in Figure 2 means the maximum efficiency

decreases. In fact, from our simulations, the maximum efficiency drops from 41 to 22% when the concentration decreases from 1 to 0.1 mM for a slip length of 90 nm.

For low concentrations without access resistance, as shown in Figure 6a, the "measured" streaming current $S_{str}\Delta P$ approaches a
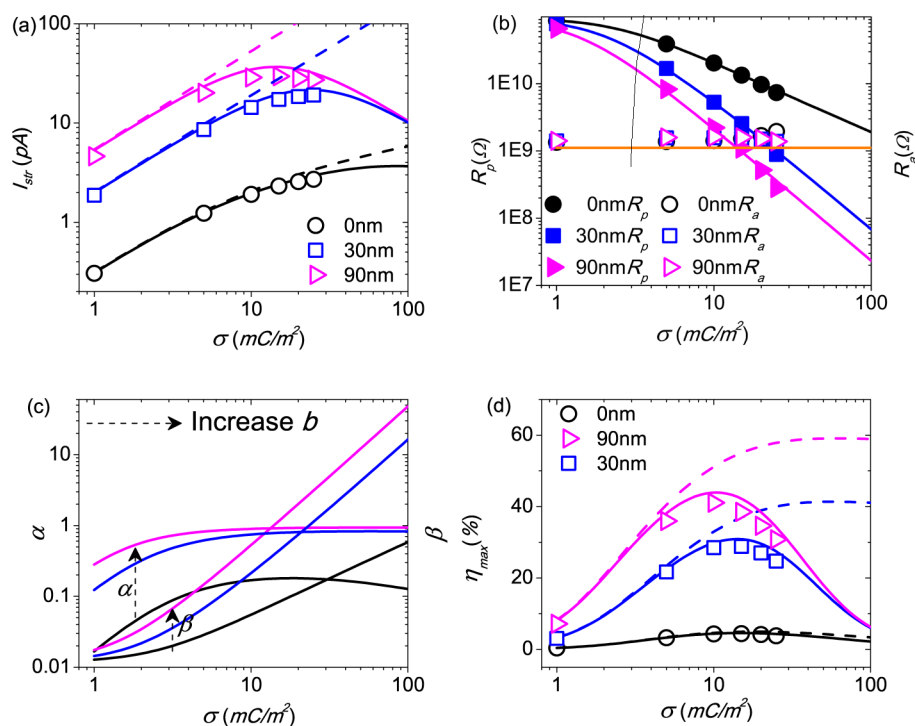
Figure 7. The dependence of the "measured" streaming current I_{str}, pore resistance R_p (closed symbols, lines), access resistance R_a (open symbols, orange line), figure of merit α, access resistance to pore resistance ratio β, and maximum efficiency η_{max} on the surface charge σ: the symbols are from numerical simulations, the dashes from the model without access resistance, and the solid lines from the model with access resistance. Three different slip lengths are used: 0 nm (black circles), 30 nm (blue squares), and 90 nm (magenta triangles). A finite optimum surface charge density occurs with the introduction of access resistance.

constant, as the concentration profile within the nanopore is controlled by the surface charge and is independent of the bulk ionic strength, as the Debye length at low concentrations exceeds the pore radius. However, as the access resistance is dependent on the bulk ionic strength, the measured streaming current no longer approaches a constant at low bulk salt concentrations but approaches zero. This is an important effect of access resistance and is why an optimum ionic strength exists. Consequently, the streaming conductance, the merit of figure (constant α), and the efficiency all approach constant values at low concentrations without access resistance. In contrast, with access resistance, the "measured" streaming current decreases at low concentrations as access resistance becomes more important, as shown in Figure 6b. Therefore, with access resistance, η_{max} decreases with respect to the salt concentration after reaching a maximum.

For high concentrations, the access resistance is much less than the nanopore resistance and is hence not significant (Figure 6b). The net charge concentrates near the region near the wall where the velocity is lowest, so the streaming conductance decreases (small S_{str} and small α). However, for a 30 nm nanopore with a slip of 30 (90) nm, the velocity due to slip is 80 (92)% of the total average velocity. Hence, the decrease in streaming conductance is small for large slip lengths. Moreover, high salt concentration C_s means more co-ion inside the nanopore (small R_p, small α), which consumes energy to overcome increased Ohmic dissipation and the percent of dissipated energy through the pore increases. As a combination of these effects, the efficiency continues to decrease when C_s increases at high values.

Up to now, experimental measurements of the streaming current performed with slip nanopores have not been reported, nor has our predicted maximum efficiency at a finite ionic strength. However, our calculated results for a slip length of 0 nm

are of the same order as two sets of data measured with a slit-like silica nanochannel or with a cylindrical nanopore.[10,43] The experiments indicated that the "measured" streaming current increases first and then decreases slightly as the KCl concentration decreases. Our analysis here shows that, besides the surface charge change mechanism at low concentrations due to protonation and deprotonation explained in these papers, access resistance may also contribute to the "measured" I_{str} reduction at low concentrations, especially for the short nanopore with slip.

The optimum charge density for optimum efficiency also occurs at a specific finite value. In the next set of simulations, we vary the charge density from 1 to 100 mC/m² while fixing the KCl concentration at 1 mM, the pore radius at 30 nm, and the slip lengths at three different values, 0, 30, and 90 nm. As shown in Figure 7a, without access resistance, the "measured" streaming current $S_{str}\Delta P$ increases with the increase of surface charge as it brings in more net charge according to the local electroneutral condition (eq 24). The nanopore resistance will decrease as more ions are introduced into the nanopore (Figure 7b). Hence, the ratio of access resistance to nanopore resistance β will increase (shown in Figure 7c). That is why, with access resistance, the "measured" streaming current of a nanopore with slip first increases and then decreases with respect to charge density—like ionic strength, it exhibits a maximum with respect to surface charge concentrations.

Without slip, the maximum efficiency at first increases with the surface charge as it brings more net charge. However, at high enough surface charge, the entering counter charge will accumulate near the wall and will not contribute significantly to the streaming current, since the velocity near the wall is small but it still contributes to the dissipation of the energy. That is also
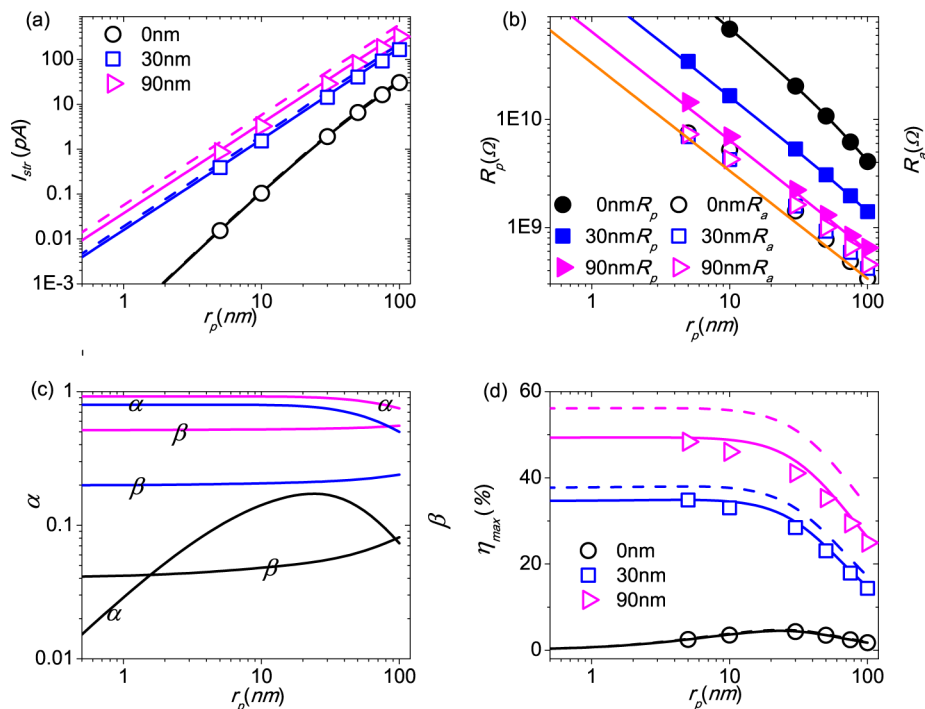
Figure 8. The dependence of the "measured" streaming current I_{str}, pore resistance R_p (closed symbols, lines), access resistance R_a (open symbols, orange line), figure of merit α, access resistance to pore resistance ratio β, and maximum efficiency η_{max} on the radius r_p: the symbols are from numerical simulations, the dashes from the model without access resistance, and the solid lines from the model with access resistance. Three different slip lengths are used: 0 nm (black circles), 30 nm (blue squares), and 90 nm (magenta triangles).
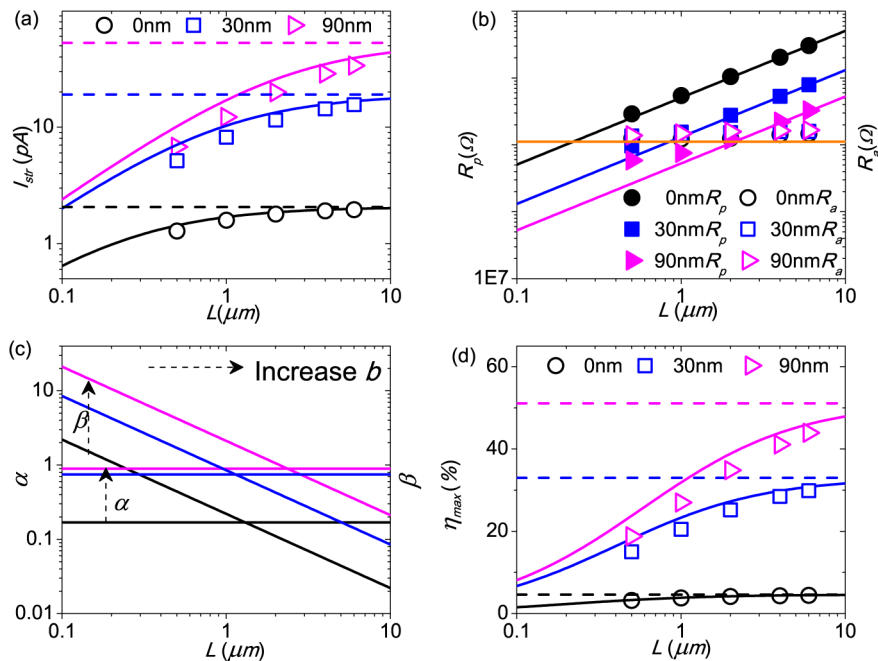
Figure 9. The dependence of the "measured" streaming current I_{str}, pore resistance R_p (closed symbols, lines), access resistance R_a (open symbols, orange line), figure of merit α, and access resistance to pore resistance ratio β and maximum efficiency η_{max} on the nanopore length L: the symbols are from numerical simulations, the dashes from the model without access resistance, and the solid lines from the model with access resistance. Three different slip lengths are used: 0 nm (black circles), 30 nm (blue squares), and 90 nm (magenta triangles).

why the figure of merit α decreases at high surface charge (same S_{str} and small R_p) with the no slip condition in Figure 7c, so is the efficiency. With slip condition and at high surface charges, however, the entering charge is at the surface and the figure of merit can be estimated to be $\alpha \sim 4b/(r_p + 4b)$, which has a value of 80 (92.3)%, compared to 81 (83.4)% from the theory at 100

mC/m^2 for a slip length of 30 (90) nm. This is also why, with large slip lengths, α is almost constant (Figure 7c). However, β increases with surface charge; hence, the larger conductance of a more charged nanopore begins to divert useful current from the load to reduce the efficiency. Hence, the maximum efficiency decreases.
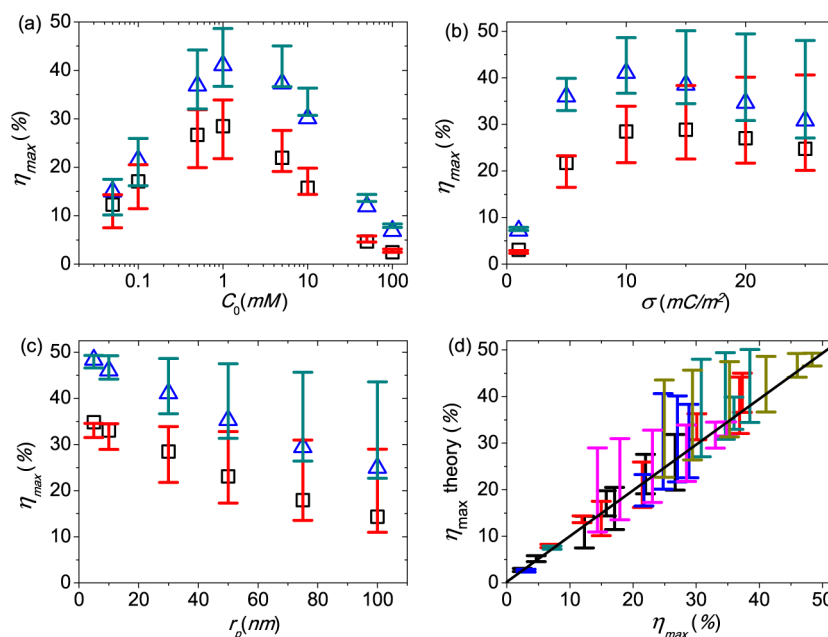
Figure 10. The collapse of data (from Figures 6−8) for the maximum efficiency from simulations (symbols) with eqs 19 and 20 and eqs 27 and 29 as the upper limit for the error bar (works better for small concentration, low surface charge, and small radius) and eqs 19 and 20 and eqs 28 and 29 as the lower limit (works better for high concentration, high surface charge, and large radius) for different concentration, surface charge, and radius. Two different slip lengths are used: 30 nm (black squares), 90 nm (blue triangles). (a, c) Both the lower limit and higher limit of the error bars give the same trend as the simulation (symbols). (b) The lower limit the error bars give the same trend as the simulation (symbols). (d) Comparison of predicted and simulated maximum efficiency for all simulations in parts a−c. Overall, the lower limit theory works better for most cases we study.

In summary, the energy conversion efficiency is very sensitive to the surface charge density of the nanopore and a higher σ does not necessarily mean a higher efficiency. There exists an optimal charge density to enable the nanofluidic battery device to have a maximum efficiency.

Pore size is also an important geometric parameter for the nanopore. In our calculation, the pore radius r_p is varied from 0.5 to 100 nm, the salt concentration is fixed at 1 mM, the surface charge density is fixed at 10 mC/m^2, and the slip length again takes on three values, 0, 30, and 90 nm. The results are shown in Figure 8.

Streaming current always increases with the radius of the nanopore as the average velocity increases with radius. As the concentration is in the surface charge dominated region $2\sigma/zFC_0r_p \gg 1$,[8] both the access and nanopore resistance decrease linearly with radius (Figure 8b) and hence β is almost constant (Figure 8c) for small radius. A smaller radius has the same effect as decreasing the concentration—it will bring more percent net charge to the center and decrease the co-ion, hence the dissipation of energy, so the maximum efficiency increases. However, for extremely small radius, only counterions can exist in the nanopore and the potential profile tends to be constant within the cross section. For small nanopores with slip ($r_p \ll b$), the figure of merit will approach $\alpha \sim (\sigma b/\mu)/(FzD/RT + \sigma b/\mu)$, which has a value 79.0 (91.84)%, compared to the simulated values of 79.6 (92.1)% for a pore 5 nm in radius with a slip length of 30 (90) nm. For nanopores without a slip of extremely small radius, $S_{str} \sim r_p^3$, $R_p \sim 1/r_p$, and $Z_p \sim 1/r_p^4$. Hence, $\alpha \sim r_p$ and the maximum efficiency decreases with radius for small r_p and approaches zero.

Length is the other important geometric parameter. In this calculation, the length varies from 0.5 to 6 μm, the salt concentration is fixed at 1 mM, the surface charge density is fixed at 10 mC/m^2, and the slip lengths are 0, 30, and 90 nm. The

pressure gradient is kept constant here as 20 kPa/μm. The results are shown in Figure 9. As expected, the length will not change the access resistance or figure of merit. Thus, a long nanopore will result in a small β and the effect of access resistance is less important. Hence, the maximum efficiency will increase until it saturates beyond a critical length. However, a pore length shorter than the critical value is often preferred, at the same applied pressure, as it corresponds to a higher power density ($I \sim 1/L$, $R \sim L$, $I^2R \sim 1/L$).

Finally, since the above analysis is mostly numerical, we offer below an estimate of the maximum efficiency for large slip lengths. For large slip $b \gg r_p$, both the pressure-driven flow and EOF profiles are flat and the figure of merit can be estimated as

$$\alpha_{up} \sim \frac{2\sigma^2 bRT}{\mu z^2 F^2 Dr_p C_0 \sqrt{X^2 + 4} + 2\sigma^2 bRT} \tag{27}$$

Here, the surface charge σ may be a function of ion strength, pH, pore size, and dissociation constant pK[42] due to protonation and deprotonation. Since the constant flow profile assumption ignores viscous dissipation, this expression always overestimates α (as an upper bound). However, for high concentration (characterized by $r_p \gg \lambda_D$) and high surface charge (characterized by $r_p \gg \lambda_{GC}$, where $\lambda_{GC} = 2\varepsilon RT/\sigma Fz$ is the Gouy−Chapman length), most space charge is in the region near the wall. If all the space charges are assumed to be at the wall, α can be estimated as

$$\alpha_{low} \sim \frac{4b}{r_p + 4b} \frac{2\sigma^2 bRT}{\mu z^2 F^2 Dr_p C_0 \sqrt{X^2 + 4} + 2\sigma^2 bRT} \tag{28}$$

which will set the lower bound for the estimate. In both cases, the access resistance to pore resistance ratio can be estimated as

8059

dx.doi.org/10.1021/jp400238v | J. Phys. Chem. C 2013, 117, 8050−8061

$$\beta \sim \frac{RT}{4z^2F^2Dr_pC_0} \left(\frac{z^2F^2D\pi r_p^2C_0\sqrt{X^2+4}}{RTL} + \frac{2\pi r_p\sigma^2 b}{\mu L} \right)$$

$$(29)$$

Figure 10 shows the collapsed data for the maximum efficiency from all the simulations by eqs 19 and 20 and eqs 27 and 29 as the upper limit for the error bar and eqs 19 and 20 and eqs 28 and 29 as the lower limit. Figure 10d shows that the low limit fits the data better as most cases are in the region $r_p \gg \lambda_{GC}$ (with the Gouy–Chapman length of 3.6 nm for 10 mC/m^2). Figure 10a–c shows that the lower limit is in better agreement with the trend in the simulations (symbols). It works well even when $r_p \sim b$. Hence, we can use eqs 19 and 20 and 27–29 to optimize the surface charge and concentration.

DISCUSSION

The above calculations and analyses indicate that slip can greatly improve the efficiency of the nanofluidic battery system. However, the inclusion of access resistance implies that the optimum ionic strength and surface charge density lie at specific finite values, because of the effect of EOF in reducing the nanopore resistance. On the basis of our theory and analytical analysis, one optimal condition for energy conversion is a pore radius of 5 nm, a KCl concentration of 1 mM, a surface charge density (like silica) of 10 mC/m^2, and a pore length of 4 μm. If the slip length is 90 nm, η_{max} is as high as 50% for such an optimized nanopore. If the slip length is at a more reasonable value of 30 nm for charged pores, η_{max} can still be as high as 35%. We suspect such a high-charge density and high-slip surface can be produced by introducing hydrophobic roughness or surfactants, like absorbed and collapsed polymer molecules, onto charged hydrophilic surfaces and a slip length of about 30 nm can be achieved.[19,21,45] Moreover, by using ionic surfactant with long and hydrophobic hydrocarbon tails, the nanopore surface should retain its high surface charge density.[21,46,47] This is probably the most viable means of introducing slip without decreasing surface charge density for this optimum geometry. We would hence encourage experimental work in these two directions, and our theory suggests a conversion efficiency as high as 35% may be attainable for such charged nanopores with large slip lengths.

AUTHOR INFORMATION

Corresponding Author
*E-mail: jmxue@pku.edu.cn; hchang@nd.edu.

Notes
The authors declare no competing financial interest.

ACKNOWLEDGMENTS

REFERENCES

(1) Yan, L.; Zhu, S.; Ji, X.; Lu, W. Proton Hopping in Phosphoric Acid Solvated Nafion Membrane: A Molecular Simulation Study. *J. Phys. Chem. B* **2007**, *111*, 6357–6363.

(2) Devanathan, R.; Venkatnathan, A.; Rousseau, R.; Dupuis, M.; Frigato, T.; Gu, W.; Helms, V. Atomistic Simulation of Water Percolation and Proton Hopping in Nafion Fuel Cell Membrane. *J. Phys. Chem. B* **2010**, *114*, 13681–13690.

(3) Talyanskii, V. I.; Shilton, J. M.; Pepper, M.; Smith, C. G.; Ford, C. J. B.; Linfield, E. H.; Ritchie, D. A.; Jones, G. A. C. Single-Electron Transport in a One-Dimensional Channel by High-Frequency Surface Acoustic Waves. *Phys. Rev. B* **1997**, *56*, 15180–15184.

(4) Kopelevich, D. I.; Chang, H.-C. Does Lattice Vibration Drive Diffusion in Zeolites? *J. Chem. Phys.* **2001**, *114*, 3776–3789.

(5) Glavin, B. A.; Kochelap, V. A.; Linnik, T. L.; Kim, K. W.; Stroscio, M. A. Generation of High-Frequency Coherent Acoustic Phonons in Superlattices under Hopping Transport. I. Linear Theory of Phonon Instability. *Phys. Rev. B* **2002**, *65*, 085303.

(6) Glavin, B. A.; Kochelap, V. A.; Linnik, T. L.; Kim, K. W.; Stroscio, M. A. Generation of High-Frequency Coherent Acoustic Phonons in Superlattices under Hopping Transport. II. Steady-State Phonon Population and Electric Current in Generation Regime. *Phys. Rev. B* **2002**, *65*, 085304.

(7) Guttenberg, Z.; Rathgeber, A.; Keller, S.; Rädler, J. O.; Wixforth, A.; Kostur, M.; Schindler, M.; Talkner, P. Flow Profiling of a Surface-Acoustic-Wave Nanopump. *Phys. Rev. E* **2004**, *70*, 056311.

(8) Yan, Y.; Wang, L.; Xue, J.; Chang, H.-C. Ion Current Rectification Inversion in Conic Nanopores: Nonequilibrium Ion Transport Biased by Ion Selectivity and Spatial Asymmetry. *J. Chem. Phys.* **2013**, *138*, 044706.

(9) Yang, J.; Lu, F.; Kostiuk, L. W.; Kwok, D. Y. Electrokinetic Microchannel Battery by Means of Electrokinetic and Microfluidic Phenomena. *J. Micromech. Microeng.* **2003**, *13*, 963.

(10) van der Heyden, F. H. J.; Bonthuis, D. J.; Stein, D.; Meyer, C.; Dekker, C. Power Generation by Pressure-Driven Transport of Ions in Nanofluidic Channels. *Nano Lett.* **2007**, *7*, 1022–1025.

(11) Xie, Y.; Wang, X.; Xue, J.; Jin, K.; Chen, L.; Wang, Y. Electric Energy Generation in Single Track-Etched Nanopores. *Appl. Phys. Lett.* **2008**, *93*, 163116.

(12) van der Heyden, F. H. J.; Bonthuis, D. J.; Stein, D.; Meyer, C.; Dekker, C. Electrokinetic Energy Conversion Efficiency in Nanofluidic Channels. *Nano Lett.* **2006**, *6*, 2232–2237.

(13) Daiguji, H.; Yang, P.; Szeri, A. J.; Majumdar, A. Electro-chemomechanical Energy Conversion in Nanofluidic Channels. *Nano Lett.* **2004**, *4*, 2315–2321.

(14) Daiguji, H.; Oka, Y.; Adachi, T.; Shirono, K. Theoretical Study on the Efficiency of Nanofluidic Batteries. *Electrochem. Commun.* **2006**, *8*, 1796–1800.

(15) Squires, T. M.; Quake, S. R. Microfluidics: Fluid Physics at the Nanoliter Scale. *Rev. Mod. Phys.* **2005**, *77*, 977–1026.

(16) Neto, C.; Evans, D. R.; Bonaccurso, E.; Butt, H.-J.; Craig, V. S. J. Boundary Slip in Newtonian Liquids: a Review of Experimental Studies. *Rep. Prog. Phys.* **2005**, *68*, 2859.

(17) Voronov, R. S.; Papavassiliou, D. V.; Lee, L. L. Review of Fluid Slip over Superhydrophobic Surfaces and Its Dependence on the Contact Angle. *Ind. Eng. Chem. Res.* **2008**, *47*, 2455–2477.

(18) Zhu, Y.; Granick, S. Rate-Dependent Slip of Newtonian Liquid at Smooth Surfaces. *Phys. Rev. Lett.* **2001**, *87*, 096105.

(19) Zhu, Y.; Granick, S. Limits of the Hydrodynamic No-Slip Boundary Condition. *Phys. Rev. Lett.* **2002**, *88*, 106102.

(20) Rothstein, J. P. Slip on Superhydrophobic Surfaces. *Annu. Rev. Fluid Mech.* **2010**, *42*, 89–109.

(21) Bouzigues, C. I.; Tabeling, P.; Bocquet, L. Nanofluidics in the Debye Layer at Hydrophilic and Hydrophobic Surfaces. *Phys. Rev. Lett.* **2008**, *101*, 114503.

(22) Chang, C.-C.; Yang, R.-J. Electrokinetic Energy Conversion Efficiency in Ion-Selective Nanopores. *Appl. Phys. Lett.* **2011**, *99*, 083102.

(23) Pennathur, S.; Eijkel, J. C. T.; van den Berg, A. Energy Conversion in Microsystems: Is There a Role for Micro/Nanofluidics? *Lab Chip* **2007**, *7*, 1234–1237.

(24) Davidson, C.; Xuan, X. Electrokinetic Energy Conversion in Slip Nanochannels. *J. Power Sources* **2008**, *179*, 297–300.

(25) Ren, Y.; Stein, D. Slip-Enhanced Electrokinetic Energy Conversion in Nanofluidic Channels. *Nanotechnology* **2008**, *19*, 195707.

8060

dx.doi.org/10.1021/jp400238v | *J. Phys. Chem. C* 2013, 117, 8050–8061

(26) Majumder, M.; Chopra, N.; Andrews, R.; Hinds, B. Nanoscale Hydrodynamics: Enhanced Flow in Carbon Nanotubes. *Nature* **2005**, *438*, 930.

(27) Whitby, M.; Cagnon, L.; Thanou, M.; Quirke, N. Enhanced Fluid Flow through Nanoscale Carbon Pipes. *Nano Lett.* **2008**, *8*, 2632−2637.

(28) Wang, L.; Friesner, R. A.; Berne, B. J. Competition of Electrostatic and Hydrophobic Interactions between Small Hydrophobes and Model Enclosures. *J. Phys. Chem. B* **2010**, *114*, 7294−7301.

(29) Hall, J. Access Resistance of a Small Circular Pore. *J. Gen. Physiol* **1975**, *66*, 531−532.

(30) Vlassiouk, I.; Smirnov, S.; Siwy, Z. Ionic Selectivity of Single Nanochannels. *Nano Lett.* **2008**, *8*, 1978−1985.

(31) Chang, C.-C.; Yang, R.-J. Electrokinetic Energy Conversion in Micrometer-Length Nanofluidic Channels. *Microfluid. Nanofluid.* **2010**, *9*, 225−241.

(32) Ben, Y.; Chang, H.-C. Nonlinear Smoluchowski Slip Velocity and Micro-Vortex Generation. *J. Fluid Mech.* **2002**, *461*, 229−238.

(33) Yossifon, G.; Mushenheim, P.; Chang, Y.-C.; Chang, H.-C. Eliminating the Limiting-Current Phenomenon by Geometric Field Focusing into Nanopores and Nanoslots. *Phys. Rev. E* **2010**, *81*, 046301.

(34) Chang, H.-C.; Yossifon, G. Understanding Electrokinetics at the Nanoscale: A Perspective. *Biomicrofluidics* **2009**, *3*, 012001.

(35) Chang, H.-C.; Yossifon, G.; Demekhin, E. A. Nanoscale Electrokinetics and Microvortices: How Microhydrodynamics Affects Nanofluidic Ion Flux. *Annu. Rev. Fluid Mech.* **2012**, *44*, 401−426.

(36) Xuan, X.; Li, D. Thermodynamic Analysis of Electrokinetic Energy Conversion. *J. Power Sources* **2006**, *156*, 677−684.

(37) Gross, R. J.; Osterle, J. F. Membrane Transport Characteristics of Ultrafine Capillaries. *J. Chem. Phys.* **1968**, *49*, 228−234.

(38) de Groot, S. R.; Mazur, P. *Non-Equilibrium Thermodynamics*; North-Holland: Amsterdam, The Netherlands, 1962.

(39) Rice, C. L.; Whitehead, R. Electrokinetic Flow in a Narrow Cylindrical Capillary. *J. Phys. Chem.* **1965**, *69*, 4017−4024.

(40) Petsev, D. N.; Lopez, G. P. Electrostatic Potential and Electroosmotic Flow in a Cylindrical Capillary Filled with Symmetric Electrolyte: Analytic Solutions in Thin Double Layer Approximation. *J. Colloid Interface Sci.* **2006**, *294*, 492−498.

(41) Plouraboué, F.; Chang, H.-C. Symmetry Breaking and Electrostatic Attraction between Two Identical Surfaces. *Phys. Rev. E* **2009**, *79*, 041404.

(42) Behrens, S. H.; Grier, D. G. The Charge of Glass and Silica Surfaces. *J. Chem. Phys.* **2001**, *115*, 6716−6721.

(43) Xue, J.; Xie, Y.; Yan, Y.; Ke, J.; Wang, Y. Surface Charge Density of the Track-Etched Nanopores in Polyethylene Terephthalate Foils. *Biomicrofluidics* **2009**, *3*, 022408.

(44) Happel, J.; Brenner, H. *Low Reynolds Number Hydrodynamics*; Prentice-Hall: Englewood Cliffs, NJ, 1965.

(45) Cheikh, C.; Koper, G. Stick-Slip Transition at the Nanometer Scale. *Phys. Rev. Lett.* **2003**, *91*, 156102.

(46) Xie, Y.; Xue, J.; Wang, L.; Wang, X.; Jin, K.; Chen, L.; Wang, Y. Surface Modification of Single Track-Etched Nanopores with Surfactant CTAB. *Langmuir* **2009**, *25*, 8870−8874.

(47) Paria, S.; Khilar, K. C. A Review on Experimental Studies of Surfactant Adsorption at the Hydrophilic Solid-Water Interface. *Adv. Colloid Interface Sci.* **2004**, *110*, 75−95.